

Far-Field Predictions from Near-Field Measurements Using an Exact Integral Equation Solution

Rédouane Laroussi and George I. Costache, *Senior Member, IEEE*

Abstract— This paper presents a new approach to derive far-field data needed in antenna and EMI/EMC testing from near-field measurements. An exact integral equation solution to the wave propagation problem is used to transform the near-field data to the far field. The method requires near-field measurements on two closed surfaces enclosing all sources and inhomogeneities. The approach is validated with numerical simulation of measurements of fields radiated from a known antenna.

I. INTRODUCTION

CHARACTERIZATION of interference from electronic equipment is a problem of great interest to the EMI/EMC community. In fact, in order for electronic equipment to be approved for use, it must comply with stringent emission regulations contained in the FCC Part 15 rules for the US and such other directives as the 89/336/EEC for the EC and the VCCI program in Japan. Compliance with emission regulations requires that the radiations from electronic equipment be fully characterized when the equipment is operating in normal conditions. These regulations, among other things, require that the radiated parasitic field levels be kept under specified maxima over a range of distances. Depending on the device under test (DUT), these distances can fall anywhere between the near field (NF) and the far field (FF) of the DUT. It is possible to transform emitted field levels obtained from one initial set of field measurements in the vicinity of the radiating equipment to any distance away from it. The theory and the best manner to proceed to achieve this transformation depend on many factors. In fact, several approaches, depending on configuration, nature of DUT, etc., have been developed to predict far-field values from near-field measurements. This is especially true in the area of antenna characterization. In the literature, the algorithm is known as the near-field to far-field transform. The advantages to such an approach are numerous. The amount of measurement data is reduced to only one set in the NF from which the rest of the information can be computed. The extent of the areas that have to be scanned to sample the field are much smaller when they are closer to the DUT (i.e., NF) than when they are in the FF. The computed results can also pinpoint localized maxima that may otherwise never be identified with direct measurements in the far field. The computation of FF from NF measurements

bypasses the problems and requirements of direct far-field measurements such as open range, good characterization of the site attenuation, and logistic problems.

Both in EMI/EMC testing and antenna characterization, the radiation takes place in homogeneous space. The analysis in homogeneous space simplifies greatly the theoretical part of deriving an NF-FF transform algorithm. In most cases, however, due to the complexity of the radiating structure itself, the algorithm has to be implemented numerically. Bucci has explored the possibility of calculating the far field from near-field amplitude measurements only [1]. The algorithm developed requires amplitude measurements on two near-field surfaces enclosing the source and derives a solution by optimizing a functional. While the accuracies achieved are very good, they depend strongly on the separation between the surfaces and any *a priori* knowledge of the radiator and phase. The algorithm also suffers from convergence and secondary minima trapping in its search for a solution. Sarkar used equivalent surface currents reconstructed from the field measurements on a sphere enclosing the antenna to compute the field outside [2]. The method solves a matrix system to obtain the current densities and computes the far field from these currents via an integral over the surface and the Green's function. Wang examined the effects of the different parameters in antenna measurements and how they affect FF pattern reconstruction by mode-sensitive algorithms [3]. Although the analysis was made for planar measurements, his conclusions are valid for any type of configuration. One major deduction is that the guidelines for measurements such as sampling rate, distance of measurements surface, and so forth are overly restrictive when there is *a priori* knowledge about the antenna. However, in a general case which would include parasitic radiation (EMI), this information may not be available and sampling rates, for instance, have been as high as five times Nyquist's. Thal worked on the optimization of the measurement parameters to reduce the amount of data for a spherical configuration [4]. This problem is a serious one since the amount of data required can be too large to handle for some algorithms as the frequency increases. The numerical results obtained are based on the Fourier transformation of reconstructed modes. Narasimhan [5], in his paper, evaluated the transform integrals using the FFT and developed techniques to improve the accuracy at the cost of more computing time.

The method proposed in this paper is derived from Green's second identity for vector fields and its development does not use any simplification. The algorithm assumes that the field

Manuscript received February 23, 1993; revised February 21, 1994.

R. Laroussi was with the Department of Electrical Engineering, University of Ottawa, Ottawa, Ont., Canada, K1N 6N5. He is now with Bell-Northern Research Laboratories, Ottawa, Ont., Canada.

G. I. Costache is with the Department of Electrical Engineering, University of Ottawa, Ottawa, Ont., Canada, K1N 6N5.

IEEE Log Number 9401878.

0018-9375/94\$04.00 © 1994 IEEE

measurements (amplitude and phase) are available around two concentric surfaces enclosing the DUT and that the field can be interpolated between the measurement positions on the surfaces and in the volume between them. The algorithm is independent of the type of radiation. It is affected only by the amount and accuracy of the data available. An analysis can also be made to take full advantage of the special cases where *a priori* knowledge of the radiator is available. This would render the approach more efficient and can substantially reduce the amount of input data. However, in the case of EMI, where most radiation is parasitic, no information is available. The algorithm, because it does not rely on any simplification, is more general than other popular NF-FF transform techniques. The presented algorithm shares some sources of error with other transform algorithms such as those introduced by numerical operations and aliasing errors due to undersampling. It is, however, more immune to aliasing error because FFT-based algorithms assume a space-limited function to justify sampling on a finite plane only. The integral transform presented here does not. Another advantage over conventional FFT transforms is that the far-field results are available everywhere and not only at discrete points.

II. FORMULATION

The radiating electronic equipment, which in the standard EMI measurement procedure is positioned above ground and radiates in free space, will be modeled by an array of short dipoles above ground, sitting on top of a table. The table, although affecting the fields radiated, is introduced as a first attempt to illustrate normal operating conditions of the DUT. It may be made of any material and its effect could even enhance radiation. The known analytical solution of the radiating antenna [9] will provide near-field values to simulate NF measurement inputs for the algorithm. The analytical expression will also be used to generate FF values to validate the algorithm. The analytical solution of the radiating dipoles considers only the ground plane and not the table. The resulting radiated fields in a practical test will reflect all sources and inhomogeneities present. This total effect will be taken into account via the measurements on the surface enclosing all sources and inhomogeneities. The device under test will consist of an array of five short dipoles radiating in free space above a perfectly conducting plane representing ground; see Fig. 1.

The equation to solve for the electromagnetic quantities in the configuration depicted in Fig.1 is Helmholtz' wave equation. For the magnetic field, it is written as

$$\nabla^2 \vec{H} + k^2 \vec{H} = 0 \quad \text{in } V. \quad (1)$$

In (1), the phasor notation for frequency-domain analysis has been dropped to simplify notation. A time variation of $e^{j\omega t}$ is assumed. The volume V , as shown in Fig.1, is infinite and homogeneous. It is bounded on one side by the surface S and the ground plane S_g . On the surface S , the magnetic field values of \vec{H} are known through field measurements, or in this case, through numerical simulation of the field measurements using the analytical field expressions of the

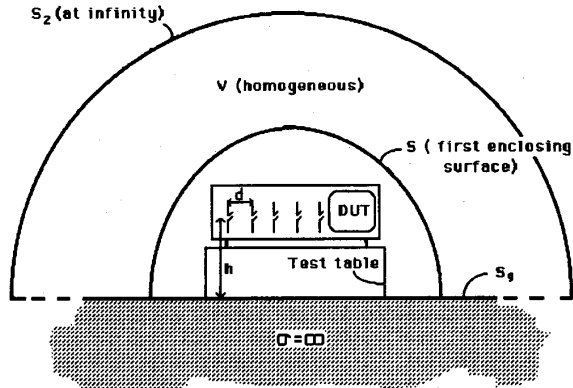


Fig. 1. Two-dimensional sketch of DUT and testing configuration.

dipoles. The surface S_2 completes the definition of the volume V . At infinity, all fields on S_2 have decayed to zero. This fact allows it to be simplified in the formulation. The conditions above on S , S_g , and S_2 fully define the boundary conditions on the solution domain. Equation (1) can be solved in several ways using numerical techniques such as Finite Element Method (FEM) and Finite Difference-Time Domain (FD-TD). However, because of the large size of solution domain required for a far-field solution, the most appropriate method would be an integral-equation-based solution.

Green's second identity for vector fields is given by

$$\begin{aligned} \int_V (\vec{Q} \cdot \nabla \times \nabla \times \vec{P} - \vec{P} \cdot \nabla \times \nabla \times \vec{Q}) dV \\ = \oint_{S_1=S \cup S_2 \cup S_g} (\vec{P} \times \nabla \times \vec{Q} - \vec{Q} \times \nabla \times \vec{P}) \cdot d\vec{S}. \end{aligned} \quad (2)$$

The volume V in (2) is infinite and corresponds to the volume considered in Fig.1. The identity is valid for any two vector functions with continuous first and second derivatives. By replacing \vec{P} by the magnetic field \vec{H} and \vec{Q} by the vector function

$$\vec{Q} = \hat{a} \phi(\vec{r}, \vec{r}') = \hat{a} \frac{e^{-jk|\vec{r}-\vec{r}'|}}{|\vec{r}-\vec{r}'|} \quad (3)$$

where \hat{a} is a unit vector of arbitrary orientation, \vec{r} and \vec{r}' are, respectively, the coordinate points in the volume V and on the surface S .

The function \vec{Q} can be recognized as the Green's function representing the magnetic vector potential of a point source in a homogeneous domain. The choice of \vec{Q} as in (3) is appropriate since V will be homogeneous. Equation (2), with the above substitutions and the use of vector identities and algebraic operations, can be manipulated to give an explicit expression to evaluate the magnetic field \vec{H} or the electric field \vec{E} in Cartesian coordinates anywhere in the volume V from its field values and its derivatives on the surface S [7]. The expression for the magnetic field is given by

$$\vec{H}(\vec{r}) = \frac{1}{4\pi} \int_S (\vec{H}(\vec{r}') \frac{\partial \phi(\vec{r}, \vec{r}')}{\partial n'} - \phi(\vec{r}, \vec{r}') \frac{\partial \vec{H}(\vec{r}')}{\partial n'}) dS. \quad (4)$$

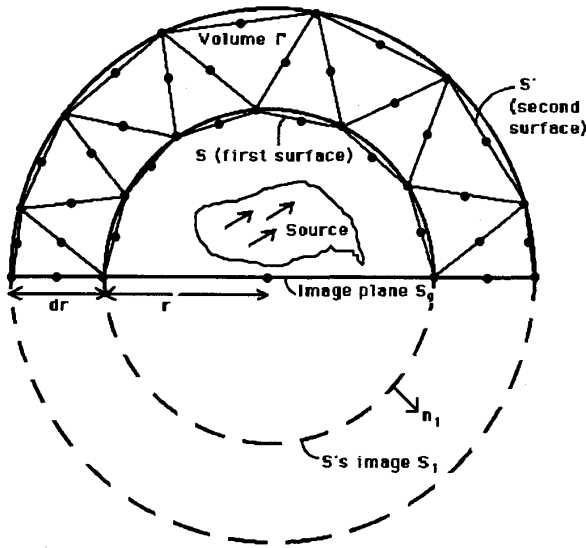


Fig. 2. Cut through the three-dimensional representation of the measurement surface, the volume Γ , and the discretization subvolumes.

For the electric field, \vec{H} is replaced by \vec{E} . The analysis that follows is done for \vec{H} . In the derivation of (4), the following assumptions have been made:

- The surface S encloses all sources and inhomogeneities.
- The primed coordinate system is for the surface S .
- The observation point \vec{r} cannot lie on the surface S .
- There are no incident fields.

III. IMPLEMENTATION

Fig. 2 represents a sketch of the model annotated with the mathematical symbols used in the implementation of (4). The problem is three-dimensional and is solved for the three Cartesian components of \vec{H} . However, for sake of clarity, the diagram in Fig.2 is shown for the equivalent 2D problem. In the 3D case, the surface S becomes a 3D spherical dome of radius r and S_g , an annulus. There are no restrictions on the radius from the point of view of the theory. The choice of r is determined by the minimum distance that will circumscribe the radiating equipment and its reactive region (usually about one wavelength). Under the assumption that the ground plane delimited by S_g is a perfect conductor, image theory can be used to obtain a closed surface around the source by extending S with its image S_1 . This will also justify the use of the free-space Green's function given in (3), reduce the measurements to a half sphere, and eliminate the need for measurements under the DUT where there are less accessible areas. The surface S_1 is closed when the contours of S , S_g , and S_2 are followed. Another way to close S_1 is to integrate over S and its image. In the process, S_2 is dropped from the integral because at infinity all quantities have decayed to zero. The contributions from S_g cancel out due to the integration in both senses.

The integral in (4) has to be evaluated numerically. The procedure requires that the vector magnetic field as well as

its derivatives be known on S and its image. To obtain the values of \vec{H} and its derivatives on S , the field is measured on two surfaces: S —the sphere of radius r , and a second surface S' —concentric to S of radius $r + dr$. The field values on S and S' allow the calculation through interpolation of the magnetic field and its derivatives on the whole surface S . The surface S , the spherical surface of radius $(r + dr)$ S' , and the volume Γ contained between them have to be represented numerically to be able to compute the integral. One way is to discretize the volume Γ by finite-size regular-shaped volumes similar to the ones used in Finite Element Analysis. The coordinate points describing the discretization subvolumes will provide the positions at which field measurements are to be taken as well as help define interpolation functions inside the subvolumes for the evaluation of the integral. In the example worked out in the paper, the volume Γ was discretized with tetrahedrons, four triangular-faced pyramids. The bases of these pyramids define the surfaces S and S' . The measurement points or nodes are placed at the vertices of the tetrahedrons and halfway on their edges as in Fig.3. The number of points per subvolume determines the order of the interpolation function inside each subvolume. The interpolation is based on a second-order interpolation expressed in terms of the field values at ten nodes and polynomials function of the local coordinates δ_1 , δ_2 , δ_3 , and δ_4 of the subvolume [8]. The interpolatory function for the x component of the magnetic field can be expressed as

$$H_x = \sum_{i=1}^{10} h_{xi} \alpha_i(\delta_1, \delta_2, \delta_3, \delta_4) \quad (5)$$

where h_{xi} is the x component of the magnetic field associated with the i th node of the subvolume the field is being interpolated in. The value of the field at the i th node is associated with one of the field measurement points. Because of the second-order interpolation, a series of measurement points will form a third surface between S and S' . For the first-order interpolation, measurements are required only on S and S' . The interpolation functions in (5) are defined as

$$\begin{aligned} \alpha_1 &= 2\delta_1^2 - \delta_1 & \alpha_6 &= 4\delta_2\delta_3 \\ \alpha_2 &= 4\delta_1\delta_2 & \alpha_7 &= 2\delta_3^2 - \delta_3 \\ \alpha_3 &= 4\delta_1\delta_3 & \alpha_8 &= 4\delta_3\delta_4 \\ \alpha_4 &= 4\delta_1\delta_4 & \alpha_9 &= 2\delta_4^2 - \delta_4 \\ \alpha_5 &= 2\delta_2^2 - \delta_2 & \alpha_{10} &= 4\delta_2\delta_4. \end{aligned} \quad (6)$$

The coordinates δ_1 , δ_2 , δ_3 , and δ_4 vary from 0 to 1 and cover the whole volume of the tetrahedron. The expressions that define the local coordinates in terms of the global Cartesian coordinates are given as follows:

$$\begin{aligned} \delta_1 &= \frac{1}{3!V} \begin{vmatrix} 1 & x & y & z \\ 1 & x_2 & y_2 & z_2 \\ 1 & x_3 & y_3 & z_3 \\ 1 & x_4 & y_4 & z_4 \end{vmatrix} & \delta_2 &= \frac{1}{3!V} \begin{vmatrix} 1 & x & y & z \\ 1 & x_1 & y_1 & z_1 \\ 1 & x_3 & y_3 & z_3 \\ 1 & x_4 & y_4 & z_4 \end{vmatrix} \\ \delta_3 &= \frac{1}{3!V} \begin{vmatrix} 1 & x & y & z \\ 1 & x_1 & y_1 & z_1 \\ 1 & x_2 & y_2 & z_2 \\ 1 & x_4 & y_4 & z_4 \end{vmatrix} & \delta_4 &= \frac{1}{3!V} \begin{vmatrix} 1 & x & y & z \\ 1 & x_1 & y_1 & z_1 \\ 1 & x_2 & y_2 & z_2 \\ 1 & x_3 & y_3 & z_3 \end{vmatrix} \end{aligned} \quad (7)$$

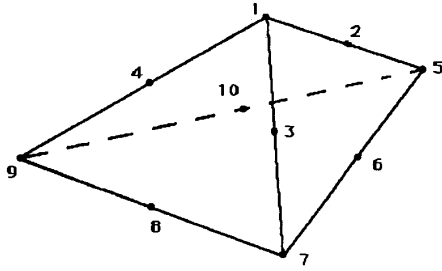


Fig. 3. Three-dimensional sketch of the discretization subvolume.

The term V is the volume of the tetrahedron. The point (x_i, y_i, z_i) refers to the Cartesian coordinates of one of the four vertices. The integral in (4) is evaluated as a summation of collocation points distributed on the surface S . The $\vec{H}(\vec{r}')$ and

$$\frac{\partial \vec{H}(\vec{r}')}{\partial n'}$$

terms are computed using (5). $\vec{H}(\vec{r}')$ is evaluated directly.

$$\frac{\partial \vec{H}(\vec{r}')}{\partial n'}$$

is evaluated using the first-order forward difference formula and (5). The terms involving Green's function are evaluated from analytical expressions. On the image portion of S , S_1 , the Green's function terms are re-evaluated with the image coordinates of \vec{r}' . The terms involving the magnetic field and its derivative are calculated from their images by a simple -1 factor multiplication of the H_z component without further computations.

From the implementation and the nature of (4), one can see that the algorithm is valid for all frequencies and does not require large execution memory. Storage memory, however, can present a problem, especially when the frequency increases. Storage is required for the discretization of the volume which will need to get finer as the frequency increases. Storage of the coordinates for measurement purposes and their interpolation association will use more and more memory. This shortcoming can be remedied since the shape of the volume V is known. Discretization data can then be generated on a need basis without storage. The other storage requirement for the actual measurement data is unavoidable.

IV. RESULTS

The field measurements that define the function $\vec{H}(\vec{r}')$ at the points provided by the discretization of S , S_1 , and Γ were simulated by sampling the analytical solution of the field radiated by the array of short dipoles (see Fig. 1). The dipoles are along the x -axis a distance $d = 0.158$ m apart, a height $h = 0.60$ m above ground, and have a phase difference of $n0.9\pi$ rad ($n = 0, \dots, 4$). The excitation frequency was 300 MHz in one simulation and 850 MHz in the other. The discretization of the spherical dome of radius $r = 1.0$ m, S was covered by 4000 triangular facets (the bases of the tetrahedrons). The outer dome S' at $r = (1.0 + 0.05)$ m,

required 4832 facets. The volume Γ required a total of 10820 tetrahedric subvolumes. The average area of the collocation point was 3.125×10^{-4} m², and the average distance between two measurement points was 2.5×10^{-2} m or 14 points per wavelength for $f = 850$ MHz. In all, measurements were simulated at 24071 points evenly distributed on the surfaces S , S_1 , and the volume Γ . Each point had three magnitudes and three phases for three Cartesian components of \vec{H} . To provide a first measure of the sensitivity of the algorithm, a simple first test has been implemented by introducing errors in the input simulated measurement values. Runs were executed at 300 MHz with corrupted and uncorrupted input values for $\vec{H}(\vec{r}')$. Computation time was of 63 s for the first set of far-field values and negligible for subsequent values. The saving in time for the subsequent runs is due to the fact that computations for $\vec{H}(\vec{r}')$ and its derivatives (the most time-consuming process) is done only once per batch of far-field values. Figs. 4–7 show a sample of the input field values at two aspect angles at $f = 300$ MHz. Because the dipoles are z -oriented, only H_x and H_y are plotted. The calculated output for the z component was exactly zero for uncorrupted zero input and decayed noise when corrupted input was used. The corrupted signal was obtained by superimposing on the analytical uncorrupted values a pseudo-random noise signal of ± 1 V maximum amplitude for a maximum signal of 10 V. Figs. 8–11 show the accuracy of the fit obtained at 300 MHz with uncorrupted input compared with the corrupted and analytical values. The computed results are shown at a distance of $r = 10$ m and an elevation angle of $\theta = 85^\circ$. Values of the field at any position in the far field can be calculated with the same near-field input. Both the magnitude and phase give very good results and demonstrate the robustness of the algorithm. The maximum error in the case of the corrupted results is of the order of 10% and corresponds to the maximum error introduced in the input data. The uncorrupted results have errors of less than 1%. This error can only be attributed to the numerical integration. The rectangular rule with the density of collocation points used does not match the accuracy of the field fitting achieved with the second-order interpolation and high rate of sampling. The error can be reduced by using more collocation points. Fig. 9 shows a significant error in phase around $\phi = 0^\circ$. This discrepancy can be explained by the fact that the associated magnitude of the analytical field on Fig. 8 is nil. The numerical algorithm computes very low field levels (Fig. 8) instead of nil values and ends up with an erroneous phase. A final test was executed at 850 MHz with still very good accuracy. Results are shown in Figs. 12–15. Fig. 14 shows a slightly higher error of about 6% that occurs in the high-field area where more accuracy is expected. The reason for the increased error is due to the fact that the measurement surface is too close to the radiating structure (the last element in the array). At 850 MHz, the distance from the last element in the array to the surface S is only of about 0.8λ at $\theta = 0^\circ$ and 180° (the x -axis along which the elements are aligned). The separation of 0.8λ is too close for near-field measurements [6] and for simulated measurements. A good distance is one wavelength or more. The x component shown in Fig. 12 computed at the same sampling density and at the same frequency shows errors

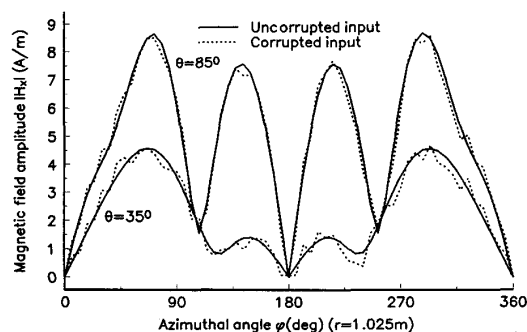


Fig. 4. Sample input to the algorithm. NF amplitude of H_x used to simulate measurements. $f = 300$ MHz.

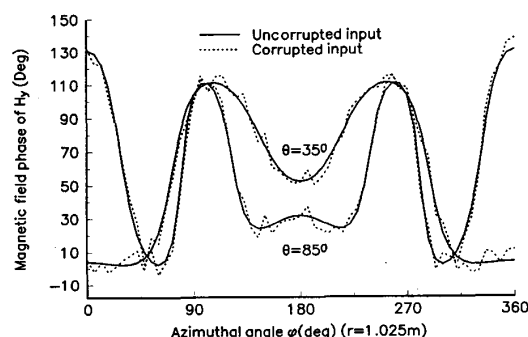


Fig. 7. Sample input to the algorithm. NF phase of H_y used to simulate measurements. $f = 300$ MHz.

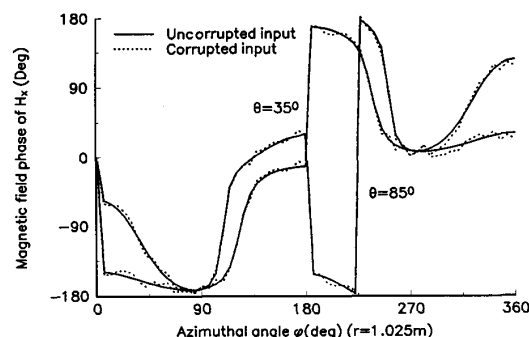


Fig. 5. Sample input to the algorithm. NF phase of H_x used to simulate measurements. $f = 300$ MHz.

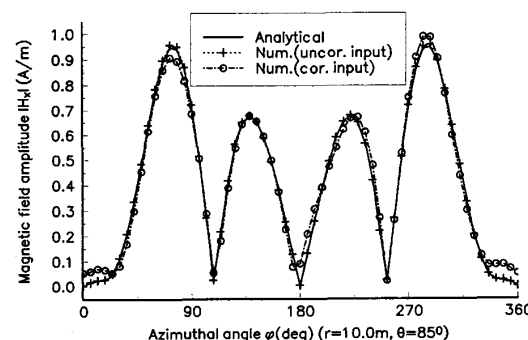


Fig. 8. Output FF amplitude for H_x using algorithm. $f = 300$ MHz.

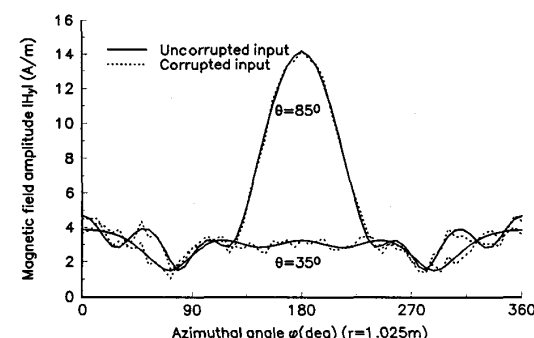


Fig. 6. Sample input to the algorithm. NF amplitude of H_y used to simulate measurements. $f = 300$ MHz.

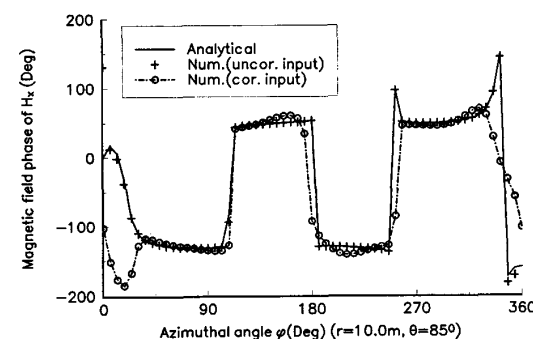


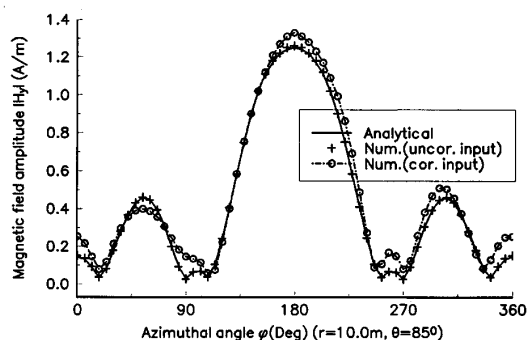
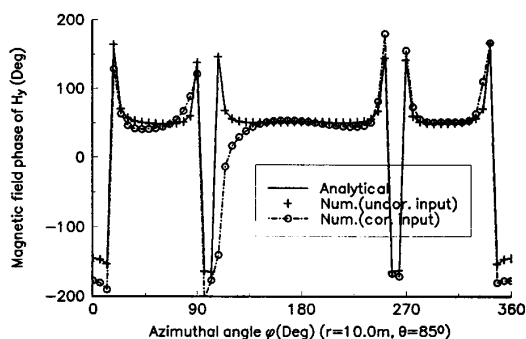
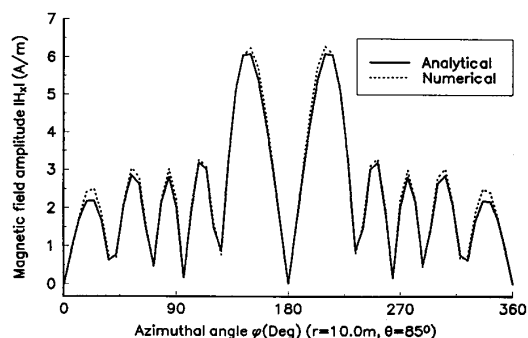
Fig. 9. Output FF phase for H_x using algorithm. $f = 300$ MHz.

in the same range of about 1%. The x component reaches its maximum at the y -axis. In that direction the measurement surface is a full 2.8λ away from the array.

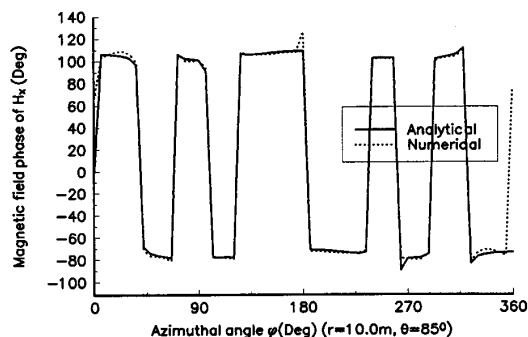
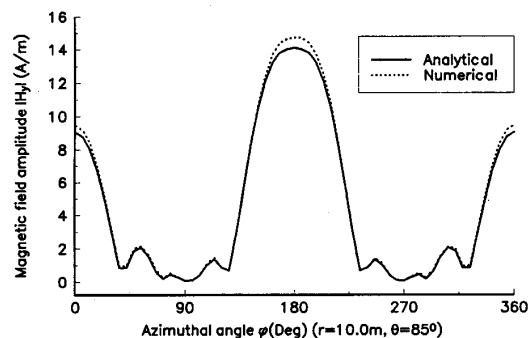
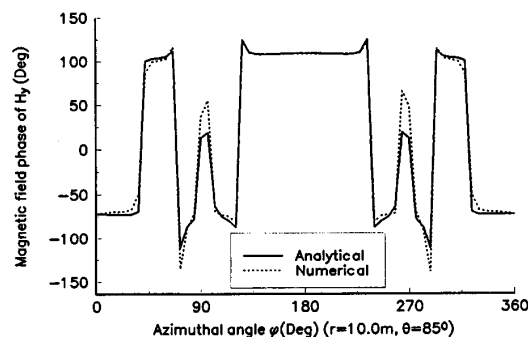
V. CONCLUSION

A method to compute far-field radiation from near-field measurements for EMI/EMC applications has been developed in this paper. It has been demonstrated that the new approach gives very good results. The algorithm has no inherent limitations as to the upper frequency bounds. It is only limited by the availability of measurements at such

high frequencies. Because the algorithm is derived from the direct numerical implementation of an exact solution of the electromagnetic propagation problem, the restrictions imposed on it are only those stemming from the numerical approach of the algorithm. There are no restrictions on the shape or size of the source enclosing surface. This is to be contrasted with series expansion schemes which are based on a coordinate system and thus give advantage to a given surface shape or the modal-determination-based algorithm which require "minimum spheres" for measurements. Unlike other methods which make use of *a priori* knowledge of the radiators or make assumptions on the nature of the radiated fields at the measurement distance, the algorithm presented here does not

Fig. 10. Output FF amplitude for H_y using algorithm. $f = 300$ MHz.Fig. 11. Output FF phase for H_y using algorithm. $f = 300$ MHz.Fig. 12. Output FF amplitude for H_x using algorithm. Uncorrputed input at $f = 850$ MHz.

rely on any shortcuts. It is developed to work with all types of radiators. This is of crucial importance in the field of EMI where the radiation is, in most cases, interference with no spatial properties. The total number of measurements and their density is reduced because the enclosing surface can be shrunk to its minimum without any adverse effects on the algorithm. The algorithms which use series expansions or mode reconstruction have a sampling rate based on the spatial rate of change of the field (modes). The sampled measurements must cover these spatial variations in order for the computed modal coefficients to be accurate. The algorithm presented does not depend on the reconstruction of these modes, it leads to believe that sampling requirements for the

Fig. 13. Output FF phase for H_x using algorithm. Uncorrputed input at $f = 850$ MHz.Fig. 14. Output FF amplitude for H_y using algorithm. Uncorrputed input at $f = 850$ MHz.Fig. 15. Output FF phase for H_y using algorithm. Uncorrputed input. at $f = 850$ MHz.

method detailed in this paper are less stringent. Although, the results, given here, were obtained from data sampled at up to five times the theoretically required rate for FFT-based algorithms, in practice, Wang has reported that for small errors, high sampling rates are required. The number of measurements can, however, be drastically reduced if a more elaborate scheme of interpolation, such as the weighted residual scheme, is implemented to interpolate data from a reduced set of measurements. Another advantage is that the Cartesian components are computed independently of each other. One can even derive the third component from the first two and thus require measurements of only two components.

Future work will improve the algorithm's efficiency by implementing more elaborate interpolation schemes and further reducing the amount of required measurement data, and by eliminating the surfaces and volume discretization storage needs. The algorithm will be validated with numerical tests of more complex antennas. Experimental tests will be conducted to investigate probe compensation requirements and actual sampling rates needed in the case of EMI.

REFERENCES

- [1] O. M. Bucci, G. D'Elia, G. Leone, and R. Pierri, "Far-field pattern determination from the near-field amplitude measurements on two surfaces," *IEEE Trans. Antennas Propagat.*, vol. 38, no. 11, Nov. 1990.
- [2] T. K. Sarkar, S. Ponnappoli, and E. Arvas, "An accurate method of computing far-field antenna pattern from near-field measurements," in *Antennas and Propagation Symp. Dig.*, vol. 1 (Dallas, TX, 1990).
- [3] J. J. H. Wang, "An examination of the theory and practices of planar near-field measurements," *IEEE Trans. Antennas Propagat.*, vol. 36, no. 6, June 1988.
- [4] H. L. Thal, Jr. and J. B. Manges, "Theory and practice for spherical-scan near-field antenna range," *IEEE Trans. Antennas Propagat.*, vol. 36, no. 6, June 1988.
- [5] M. S. Narasimhan and M. Karthikeyan, "Evaluation of Fourier transform integrals using FFT with improved accuracy and its applications," *IEEE Trans. Antennas Propagat.*, vol. AP-32, no. 4, Apr. 1984.
- [6] A. D. Yaghjian, "An overview of near-field antenna measurements," *IEEE Trans. Antennas Propagat.*, vol. AP-32, no. 1, Jan. 1984.
- [7] A. J. Poggio and E. K. Miller, "Integral equation solutions of three dimensional scattering problems," in R. Mittra, Ed., *Computer Techniques for Electromagnetics*. Oxford, UK: Pergamon, 1973.
- [8] P. P. Silvester and R. L. Ferrari, *Finite Elements for Electrical Engineers*. New York: Cambridge Univ. Press, 1990.
- [9] W. L. Stutzman and G. A. Thiele, *Antenna Theory & Design*. New York: Wiley, 1981.

Rédouane Laroussi was born in Casablanca, Morocco. He received the B.A.Sc. and M.A.Sc. degrees in electrical engineering from the University of Ottawa, Ottawa, Ont., Canada, in 1989 and 1993, respectively.

His research work is in the area of near-field to far-field transformation and absorbing boundary conditions for the Finite Element method. Presently, he is a member of the scientific staff at Bell-Northern Research Laboratories, Ottawa.

George I. Costache (M'78-SM'82) is a professor in the Electrical Engineering Department at the University of Ottawa, Ottawa, Ont., Canada. His career has included positions at Bell-Northern Research, Ottawa.; the University of Manitoba; and the Polytechnic Institute of Bucharest. He has taught electromagnetics and numerical techniques applied to electromagnetics for more than 24 years and has made original contributions to the solution of skin-effect problems and electromagnetic transient phenomena. His main interest is in numerical techniques, such as finite-element analysis and moment methods, and their application to interference problems in steady-state and time-domain applications. The author or coauthor of more than 50 technical papers and reports.

Dr. Costache is an Associate Editor of the IEEE TRANSACTIONS ON ELECTROMAGNETIC COMPATIBILITY. He is also a member of the editorial review board of *COMPEL*, the *International Journal for Computation and Mathematics in Electrical and Electronics Engineering*, the *International Journal of Numerical Modelling*, *Electronic Networks Devices and Fields*, and the IEEE TRANSACTIONS ON MICROWAVE THEORY AND TECHNIQUES. He is a Registered Professional Engineer in the Province of Ontario, Canada.